Characterization of $Na_2Zn_2TeO_6$ ceramic solid electrolyte densified by hot pressing

Akihiro Itaya, Yuki Ono, Kazuki Yamamoto, Ryoji Inada*

Department of Electrical and Electronic Information Engineering, Toyohashi University of Technology, 1-1 Hibarigaoka, Tempaku-cho, Toyohashi, Aichi 441-8580, Japan.

*Corresponding author:

Phone: +81-532-44-6723, Fax: +81-532-44-6757, E-mail address: inada.ryoji.qr@tut.jp

ORCID ID: 0000-0002-6357-092X

ABSTRACT

In this work, we applied hot pressing (HP) for the densification of $Na_2Zn_2TeO_6$ (NZTO) at lower temperature than conventional furnace sintering (FS). Calcined NZTO powder was densified by HP at 700 ºC for 1 hour under uniaxial pressure of 20 and 60 MPa using a graphite mold. By increasing the uni-axial pressure to 60 MPa for HP, high relative density above 90 % was obtained. As-prepared NZTO by HP showed total (bulk + grain-boundary) ionic conductivity of 0.29 mS cm^{-1} at room temperature, which is lower than NZTO prepared by FS at 800 ºC (= 0.4 mS cm^{-1}) with lower relative density (< 85 %). It was found that the contribution of grain-boundary resistance in as-prepared NZTO by HP is larger than NZTO by FS. We confirmed that the grain-boundary resistance was significantly reduced by post-annealing. Consequently, total conductivity at room temperature was improved to 0.42 mS cm^{-1} and 0.56 mS cm^{-1} by annealed at 700 ºC and 800 ºC for 2 hours. X-ray photoelectron spectroscopy analysis indicated the

residual carbon-contained secondary phases were reduced by post-annealing. These secondary phases could be formed by the carbon contamination from a graphite mold for HP and their removal by post-annealing results into the improvement ionic conduction at grain-boundary.

KEYWORDS: solid electrolyte, layered oxide, sodium-ion conductivity, hot-pressing

1. INTRODUCTION

All-solid-state sodium (Na) ion batteries (SiBs) are promising high-safety and low cost alternative energy storage devices to current lithium ion batteries, particularly suitable for the application to large-scale energy storage systems.[1–5] Development of inorganic solid Na-ion conducting materials used for solid electrolyte is most critical issue to realize all-solid-state SiBs. The solid electrolyte materials should have not only high Na-ion conductivity above 1 mS cm^{-1} at room temperature but also chemical and electrochemical stabilities against both positive and negative electrode active materials.[2,3] Although oxide based solid electrolyte materials have rather lower conductivity and deformability than sulfide based one, they have other advantages such as their chemical stability in air and easiness for handling.[3–5]

Na-ion conducting oxide solid electrolyte $Na_2Zn_2TeO_6$ (NZTO) with a P2-type layered structure is an attractive candidate for the application to all-solid-state SiBs, because of the high ionic conductivity well above 0.1 mS cm^{-1} at room temperature range and excellent chemical and electrochemical stability against Na metal.[6–12] NZTO has a honeycomb-structured compound with a space group of $P6_322$ and in the layers, each TeO_6 octahedron is surrounded by six ZnO_6 octahedra via edge-sharing. Na ions are

located between the layers at three different sites, all of which are partially occupied and thus Na ions can migrate among them. Interestingly, first-principles calculations display both high room temperature conductivity of 9.77 mS cm^{-1} and intrinsic and wide intrinsic electrochemical stability for NZTO.[13] In addition, the processing temperature of NZTO is much lower than other Na-ion conducting oxides such as Na-β/β" alumina, NASICON-type $Na_3Zr_2Si_2PO_{12}$, and sodium silicates $Na_5YSi_4O_{12}$.[14–23] Densification temperature and room temperature ionic conductivity for NZTO and other Na-ion and Li-ion conductive oxide solid electrolytes [24–29] are compared in Table 1.

As reported in the literature, sintering temperature for densification of NZTO is usually set to be 800–900 °C.[6–12] Although this temperature may be still high for the formation of good solid-solid interface with most electrode active materials by co-sintering process, there is a possibility to suppress the formation of undesired secondary phases by co-sintering with cathode active materials with similar crystal structure and constituent elements.[30–35] However, reported relative densities of NZTO by a conventional sintering are limited to approximately 85 %, mainly due to the non-uniformity in NZTO grain size and morphology. [6–12] Recently, aerosol deposition process without any thermal treatment was applied for fabricating NZTO thick film, but the density and conductivity were not as high as sintered samples.[36]

In this work, we applied hot pressing (HP) process for fabricating dense NZTO at lower densification temperature and shorter processing time. Microstructure and ionic conducting property of NZTO by HP are examined and compared with NZTO prepared by a conventional furnace sintering (FS).

2. MATERIALS AND METHODS

NZTO powder was synthesized via a conventional solid state reaction method. Na_2CO_3 (Kojundo Chemical Laboratory, 99.5%), ZnO (Kishida Chemical, 99.99%) and TeO_2 (Kojundo Chemical Laboratory, 99.9%) weighed with the molar ratio of Na : Zn : Te = 2.2 : 2 : 1 (adding 10% excess Na taking into account the volatilization of Na during the processing [10–12]) were mixed and ground with ethanol for 5 hours by planetary ball-milling (Nagao System, Planet M2-3F) with zirconia balls with the diameter of 10 mm in a zirconia pot. As reported in the literature, pure P2-type NZTO phase is obtained at synthesis temperature of 900 °C and lower synthesis temperature produces the O'3-type phase.[10] On the other hand, there is a possibility to form secondary phases due to the volatilization of Na during high temperature processing.[11] Therefore, we dried the mixture of precursor at 80 °C and then calcined at 850 °C for 6 hours in air using a SiC crucible. Calcined NZTO powder was reground and hot-pressed at 700 ºC for 1 hour with a graphite mold in a vacuum chamber of the furnace designed for hot pressing and spark plasma sintering (CSP-I-02121, SS Alloy Co Ltd.). The densification temperature is 100–150 ºC lower than the temperature for conventional furnace sintering in our previous works.[11,12] During the densification process, the uniaxial pressure of 20 MPa and 60 MPa was applied to a sample. After removing the pelletized NZTO sample from the graphite mold, the discolored portion of the pellet surface layer was removed by mechanical polishing with a sandpaper (grit number #800). For comparison, pelletized NZTO sample was also prepared by a conventional furnace sintering (FS). Calcined NZTO powder was pelletized by cold isostatic pressing at 300 MPa, and then sintered at 800°C for 12 hours in air using a SiC crucible.

The relative densities of all sintered NZTO were calculated by dividing the mass density by the theoretical one (= 4.88 g cm^{-3}).[6,7] The crystal phase of each sintered NZTO

was evaluated by X-ray diffraction (XRD, RIGAKU Multiflex) using Cu$K\alpha$ radiation (λ = 0.15418 nm). Microstructure of each sintered NZTO was observed by a scanning electron microscope (SEM, Keyence VE-8800). The contamination in NZTO samples from the graphite mold used in HP were characterized by using an X-ray photoelectron spectrometer (Quantera SXM, ULVAC-PHI Inc.) with an Al$K\alpha$ X-ray source (1486.6 eV). Ionic conductivity was evaluated at a temperature range from 27 to 152 °C by an AC impedance measurement with a frequency from 4 Hz to 3 MHz and an applied voltage amplitude of 0.1 V, using an impedance meter (HIOKI IM3536). Before the conductivity measurements, both parallel end surfaces of each sintered NZTO pellet were coated with Au films as ion blocking electrodes.

3. RESULTS AND DISCUSSION

Figure 1 shows X-ray diffraction (XRD) patterns for calcined NZTO powder (before densification) and hot-pressed NZTO samples with different applied uniaxial pressures. The calculated patterns for P2-type NZTO phase based on the structure data are also plotted as the reference.[6] Although the diffraction peaks of the crystal plane with a *c*-axis orientation are emphasized slightly, the peak position from main phase for both calcined powder and hot-pressed samples agrees well with the calculated pattern for P2-type NZTO phase, indicating that hot pressing in vacuum condition does not effect on the crystal structure of NZTO. For calcined NZTO powder and hot pressed NZTO at 20 MPa, a small peak near 002 reflection is confirmed, which may be attributed to NaOH phase.[11] The microstructure of fractured cross sectional surface for hot-pressed NZTO samples was observed by SEM and the results are shown in Figure 2. As can be seen, shapes and sizes of NZTO grains in both hot-pressed samples are not uniform, but the porosity in

hot-pressed samples is different depending on the applied uniaxial pressure. The sample pressure-molded at 60 MPa has fewer voids and a higher density than the one pressure-molded at 20 MPa. In fact, the relative density of the former reached 91%, while that of the latter was only 83%, nearly the same for NZTO prepared by conventional furnace sintering.[11,12]

Figure 3(A) shows the comparison of Nyquist plots for complex impedance at 27 ºC for hot-pressed NZTO densified at 60 MPa and NZTO prepared by FS. Here, Z' in a horizontal axis and Z'' in a vertical axis are the real and imaginary parts of impedance, and the units for both components are Ω cm for direct comparison among the samples with different geometrical parameters. It is evident that the plots for both samples are composed of the part of a distorted semicircle at high frequency range and a linear tail at low frequency range. These data belong to the ionic conduction at NZTO grain boundaries and the response by ionic blocking electrodes.[11,12] Since the upper limit of measurement frequency in this work was limited to 3 MHz, the data reflecting the ionic conduction in NZTO grain is not observed clearly. The values for constant phase angle element (CPE) of distorted semicircle in Nyquist plot for NZTO by FS and NZTO by HP are 7.45×10^{-8} F and 4.63×10^{-8} F, respectively. These values are close to the specific CPE value for grain boundary contribution,[37] so that the diameter of distorted semicircle corresponds to the grain-boundary resistivity R_{gb} in each sample. Although the relative density of hot-pressed NZTO was 91 % and higher than NZTO by FS (= 83 %), R_{gb} of the former seems to be much larger than the latter.

In Figure 3(A), the intercept point of an extrapolation line of the linear tail in low frequency range and horizontal Z' axis corresponds to the total (grain + grain boundary) resistivity R_{total} of each sample. Mainly due to the larger R_{gb}, hot-pressed NZTO has larger

R_{total} than NZTO prepared by FS. The total (bulk + grain-boundary) conductivity σ_{total} is calculated by the inverse of R_{total}. σ_{total} of hot-pressed NZTO is estimated to be 0.29 mS cm^{-1} at 27 ºC and lower than that for NZTO prepared by FS (= 0.40 mS cm^{-1}). Figure 3(B) shows the variation σ_{total} as a function of inverse of temperature T. It is confirmed that the temperature dependence of σ_{total} in each sample is well expressed by the Arrhenius equation $\sigma_{total}T = \sigma_0 \exp(-E_a / k_BT)$. Here, σ_0 is constant, E_a is the activation energy for σ_{total} and k_B is Boltzmann constant (= 1.381×10^{-23} J K^{-1}), respectively. E_a for both samples are nearly the same (= 0.26 eV), and close to the E_a values for NZTO (= 0.25–0.30 eV) reported in the literature.[7–12]

To modify the grain-boundary resistivity for Na-ion conduction in hot-pressed NZTO, post-annealing in air at 700 ºC or 800 ºC for 2 hours was applied to hot-pressed NZTO prepared at 60 MPa. Change in relative density of NZTO by post-annealing was within 0.5 %. Figure 4 shows XRD patterns for hot-pressed NZTO before and after applying post-annealing. The main peaks in hot-pressed NZTO after post-annealing are indexed as P2-type NZTO phase. In sample annealed at 700 ºC, several minor peaks (marked by triangles) are detected at 2θ = 16.5 º and 32–41 º, possibly due to the formation of O'3 NZTO phase.[10] The detailed mechanism for the formation of O'3 phase by post annealing at 700 ºC is under investigation.

Figure 5 shows X-ray photoelectron (XPS) spectra measured on a fractured cross sectional surface of hot-pressed NZTO before and after post-annealing at 800 ºC. As shown in Figure 5(A), the XPS spectra of both samples are almost identical except for the C1s peak. It is clearly confirmed that the intensity for C1s peak is reduced remarkably after post-annealing. Enlarged C1s spectra in hot-pressed NZTO before and after post-annealing are plotted in Figure 5(B) and (C). Before applying post-annealing (Figure

5(B)), C1s spectra is composed of large contribution of C–C bonding (284.2 eV) and small contribution O–C=O bonding (288.5 eV), suggesting that carbon is contained as main secondary phase in hot-pressed NZTO, which comes from a graphite mold used in densification process. The contribution of C–C bonding is still dominant after post-annealing, but its fraction is decreased significantly and the fraction of O–C=O bonding and C–O bonding (286.1 eV) are increased (Figure 5(C)). These carbon-based impurities remain on the NZTO grain surface, and are presumed to be a factor that inhibits Na-ion conduction between NZTO grains.

To examine the effect of post-annealing on ionic conducting properties in hot-pressed NZTO, we measured complex impedance of hot-pressed NZTO after post-annealing. Figure 6(A) is the change in Nyquist plots for complex impedance at 27 ºC for hot-pressed NZTO before and after applying post-annealing. The dashed line in Figure 6(A) represents the fitting curve for the equivalent circuit consisting of $(R_b)(R_{gb}–Q_{gb})(Q_{el})$, where R_b, R_{gb}, Q_{gb} and Q_{el} correspond to the bulk resistance, grain-boundary resistance, CPE of grain boundary and electrodes. Bulk resistivity R_b and R_{gb} for hot-pressed NZTO before and after post-annealing were estimated from the fitting based on equivalent circuit model. The obtained results are summarized in Figure 6(B). It is found that the change in R_b by post-annealing are small, suggesting the influence of post-annealing on the ionic conducting property in NZTO grain is negligible.

Q_{gb} values for hot-pressed NZTO after annealed at 700 ºC and 800 ºC are estimated to 1.84×10^{-8} F and 1.11×10^{-8} F. These values are slightly lower than hot-pressed NZTO without post annealing (= 4.63×10^{-8} F), but close to the specific values for grain-boundary contributuion.[37] R_{gb} is significantly reduced by post-annealing and its temperature. R_{gb} shows the highest value (= 2433 Ω cm) in hot-pressed sample without

post-annealing, but is decreased to 1449 Ω cm and 870 Ω cm by post-annealing at 700 ºC and 800 ºC. It is noted that NZTO prepared by FS at 800 ºC has R_b = 966 Ω cm and R_{gb} = 1353 Ω cm. The fraction of R_{gb} in R_{total} (= R_b + R_{gb}) shows the lowest value (= 0.49) in hot-pressed NZTO after post-annealing at 800 ºC, which is smaller than the value for NZTO prepared by FS (= 0.58). The reduction of R_{gb} in hot-pressed NZTO by post-annealing is correlated well to the decrease in carbon-based secondary phase after post-annealing.

Bulk and total ionic conductivity σ_b and σ_{total} at 27 ºC for hot-pressed NZTO samples with or without post-annealing is calculated by R_b and R_{total} value and summarized in Figure. 7(A). The calculated results of σ_{bulk} and σ_{total} for NZTO prepared by FS are also plotted for comparison. It is evident that the difference in σ_b among the all samples is very small and the values are ranged from 1.03 mS cm^{-1} to 1.1 mS cm^{-1}. On the other hand, σ_{total} is increased from 0.29 mS cm^{-1} to 0.42 mS cm^{-1} and 0.56 mS cm^{-1} by applying post-annealing at 700 ºC and 800 ºC, due to the decrease in R_{gb} contribution by post-annealing as mentioned above. Both are higher than NZTO by FS at 800 ºC, but to discuss the difference in σ_{total} values among the samples further, the difference in relative density should be considered. Wu et al have reported about the calibration of conductivity for sintered NZTO samples corrected for porosity according to the Bruggeman symmetric model for the 3–3 connectivity of spherical grains and pores (assuming the latter to have zero conductivity).[8] In this model, true conductivity σ_t is expressed as $\sigma_t = \sigma_c / (1 - 1.5f_{pore})$, where σ_c is the conductivity of porous ceramic body and f_{pore} is the fraction of pore in a sample.[38,39] Using this relational expression, σ_{total} for NZTO by FS and hot-pressed NZTO after annealed at 800 ºC is calibrated to 0.54 mS cm^{-1} and 0.65 mS cm^{-1}.

Even considering the difference in relative density, σ_{total} of the latter is approximately 20% higher than that of the former. Figure. 7(B) shows the Arrhenius plots for hot-pressed NZTO with and without post annealing. It is found that the magnitude relationship of σ_{total} among the samples does not change within the measurement temperature range. E_a showed the lowest value (= 0.24 eV) in hot-pressed NZTO after post-annealed at 800 ºC, which is attributed to the lowest contribution of R_{gb} in R_{total} among the all samples.

4. CONCLUSION

In summary, we applied hot pressing (HP) for the densification of NZTO ceramic electrolyte at lower temperature than conventional furnace sintering (FS). Calcined NZTO powder was densified by HP at 700 °C for 1 hour under uniaxial pressure of 20 MPa and 60 MPa using a graphite mold. By increasing the applied pressure to 60 MPa for HP, high relative density above 90% was obtained. As-prepared NZTO densified by HP showed lower total ionic conductivity of 0.29 mS cm^{-1} at room temperature than NZTO prepare by FS at 800 ºC (= 0.4 mS cm^{-1}) with lower relative density. It was found that the grain-boundary resistance of NZTO by HP was significantly reduced by post-annealing in air. Total ionic conductivity at room temperature was improved to 0.42 mS cm^{-1} and 0.56 mS cm^{-1} in post-annealed samples at 700 ºC and 800 ºC. This is mainly attributed to the elimination of secondary phases formed by the carbon contamination from graphite die used for HP.

ACKNOWLEDGEMENTS

This work was partly supported by Research Grant from Iketani Science and Technology Foundation (0321104-A), Foundation of Public Interest of Tatematsu, The

Kazuchika Okura Memorial Foundation, and Grant-in-Aid for Scientific Research (JSPS KAKENHI) Grant Number 22H01468 from the Japan Society for the promotion of Science (JSPS). We acknowledged the support of the Cooperative Research Facility Center at Toyohashi University of Technology.

REFERENCES

1. Zhou W, Li Y, Xin S, Goodenough JB. Rechargeable sodium all-solid-state battery. ACS Cent Sci 2017; 3:52–57.
2. Hou W, Guo X, Shen X, Amine K, Yu H, Lu J. Solid electrolytes and interfaces in all-solid-state sodium batteries: Progress and perspective. Nano Energy 2018; 52:279–291.
3. Zhou C, Bag S, Thangadurai V. Engineering materials for progressive all-solid-state Na batteries. ACS Energy Lett 2018; 3:2181−2198.
4. Chao C, Liu L, Qi X, Lu Y, Wu F, Zhao J, Yu Y, Hu YS, Chen L. Solid-state sodium batteries. Adv Energy Mater 2018; 8:1703012
5. Ma Q, Tietz F. Solid-state electrolyte materials for sodium batteries: Towards practical applications. ChemElectroChem 2020; 7:2693–2713.
6. Evstigneeva MA, Nalbandyan VB, Petrenko AA, Medvedev BS, Kataev AA. A new family of fast sodium ion conductors: $Na_2M_2TeO_6$ (M = Ni, Co, Zn, Mg). Chem Mater 2011; 23:1174–1181.
7. Li Y, Deng Z, Peng J, Chen E, Yu Y, Li X, Luo J, Huang YY, Zhu J, Fang C, Li Q, Han J. A P2-type layered superionic conductor Ga-doped $Na_2Zn_2TeO_6$ for all-solid-state sodium-ion batteries. Chem Eur J 2018; 24:1057–1061.
8. Wu JF, Wang Q, Guo X. Sodium-ion conduction in $Na_2Zn_2TeO_6$ solid electrolytes.

J Power Sources 2018; 402:513−518.

9. Deng Z, Gu J, Li Y, Li S, Peng J, Li X, Luo J, Huang YY, Fang C, Li Q, Han J, Huang Y, Zhao Y, Ca-doped $Na_2Zn_2TeO_6$ layered sodium conductor for all-solid-state sodium-ion batteries. Electrochim Acta 2019; 298:121−126.
10. Li X, Bianchini F, Wind J, Pettersen C, Wragg DS, Vajeeston P, Fjellvåg H, Insights into crystal structure and diffusion of biphasic $Na_2Zn_2TeO_6$. ACS Appl Mater Interfaces 2020; 12:28188−28198.
11. Itaya A, Yamamoto K, Inada R, Sakurai Y. Effect of excess Na contents in precursor on the property of $Na_2Zn_2TeO_6$ ceramic solid electrolyte. Mater Lett 2020; 284:128941.
12. Itaya A, Yamamoto K, Inada R, Sakurai Y. Sintering temperature dependency on sodium-ion conductivity for $Na_2Zn_2TeO_6$ solid electrolyte. Int J Appl Ceram Technology 2021; 18:2085−2090.
13. Huang H, Yang Y, Cheng C, Wu H-H, Huang B. Phase stability and fast ion transport in P2-type layered $Na_2X_2TeO_6$ (X = Mg, Zn) solid electrolytes for sodium batteries. J Mater Chem A 2020; 8: 22816−22817.
14. Youngblood GE, Miller GR, Gordon RS. Relative effects of phase conversion and grain size on sodium ion conduction in polycrystalline, lithia-stabilized β-alumina. J Am Ceram Soc 1978; 61:86–87.
15. Lu X, Xia G, Lemmon JP, Yang Z. Advanced materials for sodium-beta alumina batteries: Status, challenges and perspectives. J Power Sources 2010; 195:2431–2442.
16. Bay MC, Wang M, Glissa R, Heinz MVF, Sakamoto J, Battaglia C. Sodium Plating from Na β-alumina ceramics at room temperature, paving the way for fast-charging

all-solid-state batteries. Adv Energy Mater 2020; 10:1902899.

17. Goodenough JB, Hong HYP, Kafalas JA. Fast Na^+-ion transport in skeleton structure. Mater Res Bull 1976; 11:203–220.

18. Noi K, Suzuki K, Tanibata N, Hayashi A, Tatsumisago M. Liquid-phase sintering of highly Na^+ ion conducting $Na_3Zr_2Si_2PO_{12}$ ceramics using Na_3BO_3 additive. J. Ame Ceram Soc 2018; 101:1255–1265.

19. Narayanan S, Reid S, Butler S, Thangadurai V. Sintering temperature, excess sodium, and phosphorous dependencies on morphology and ionic conductivity of NASICON $Na_3Zr_2Si_2PO_{12}$. Solid State Ionics 2019; 331:22–29.

20. Ma Q, Tsai CL, Wei XK, Heggen M, Tietz F, Irvine JTS, Room temperature demonstration of a sodium superionic conductor with grain conductivity in excess of 0.01 S cm^{-1} and its primary applications in symmetric battery cells. J Mater Chem A 2019; 7:7766–7776.

21. Sun G, Yang X, Chen N, Yao S, Wang X, Jin X, Chen G, Xie Y, Du F. $Na_5YSi_4O_{12}$: A sodium superionic conductor for ultrastable quasi-solid-state sodium-ion batteries. Energy Storage Mater 2021; 41:196–202.

22. Yang A, Ye R, Li X, Lu Q, Song H, Grüner G, Ma Q, Tietz F, Fattakhova-Rohlfing D, Guillon O. Fabrication of thin sheets of the sodium superionic conductor $Na_5YSi_4O_{12}$ with tape casting. Chem. Eng. J. 2022; 435:134774.

23. Sivakumaran A, Samson A J, Thangadurai V. Progress in sodium silicates for all-solid-state sodium batteries—a review. Energy Technol 2023; 11:2201323.

24. Zhang P, Wang H, Si Q, Matsui M, Takeda Y, Yamamoto O, Imanishi N. High lithium ion conductivity solid electrolyte of chromium and aluminum co-doped NASICON-type $LiTi_2(PO_4)_3$. Solid State Ion 2015; 272:101−106.

25. Zhang M, Huang Z, Cheng J, Yamamoto O, Imanishi N. Chi B, Pu J, Li J. Solid state lithium ionic conducting thin film $Li_{1.4}Al_{0.4}Ge_{1.6}(PO_4)_3$ prepared by tape casting, J Alloy Compd 2014; 590:147–152.

26. Inaguma Y, Nakashima M. A rechargeable lithium–air battery using a lithium ion-conducting lanthanum lithium titanate ceramics as an electrolyte separator. J Power Sources 2013; 228:250–255.

27. Inada R, Kimura K, Kusakabe K, Tojo T, Sakurai Y. Synthesis and lithium-ion conductivity for perovskite-type $Li_{3/8}Sr_{7/16}Ta_{3/4}Zr_{1/4}O_3$ solid electrolyte by powder-bed sintering. Solid State Ion 2014; 261:95–99.

28. Inada R, Yasuda S, Hosokawa H, Saito M, Tojo T, Sakurai Y. Formation and stability of Interface between garnet-type Ta-doped $Li_7La_3Zr_2O_{12}$ solid electrolyte and lithium metal electrode. Batteries 2018; 4:26.

29. Dai R, Avdeev M, Kim S-J, Rao P P, Adams S. Temperature dependence of structure and ionic conductivity of $LiTa_2PO_8$ ceramics, Chem Mater 2022; 34: 10572–10583.

30. Gupta A, Mullins CB, Goodenough JB. $Na_2Ni_2TeO_6$: Evaluation as a cathode for sodium battery. J Power Sources 2013; 243:817–821.

31. Yang Z, Jiang Y, Deng L, Wang T, Cheng S, Huang Y. A high-voltage honeycomb-layered Na_4NiTeO_6 as cathode material for Na-ion batteries. J Power Sources 2017; 360:319–323.

32. Xiao L, Ding Z, Cheng C, Han Z, Wang P, Huang Q, Gao P, Wei W. Insight into the structural disorder in honeycomb-ordered sodium-layered oxide cathodes. iScience 2020; 23:100898.

33. Kanyolo GM, Masese T, Matsubara M, Chen CY, Rizell J, Huang ZD, Sassa Y, Månsson M, Senoh H, Matsumoto H. Honeycomb layered oxides: structure, energy

storage, transport, topology and relevant insights. Chem Soc Rev 2021; 50:3990–4030.

34. Masese T, Miyazaki Y, Rizell J, Kanyolo GM, Takahashi T, Ito N, Senoh H, Saito T. Unveiling structural disorders in honeycomb layered oxide: $Na_2Ni_2TeO_6$, Materialia 2021; 15:101003.

35. Yamamoto K, Ono Y, Inada R. Characterization of $Na_2M_2TeO_6$ (M = Ni, Zn) for oxide-based all-solid-state sodium-ion batteries. ECS Meet Abst 2022; MA2022-01:2408.

36. Teshima S, Ono Y, Goto N, Inada R. Electrical conducting properties of $Na_2Zn_2TeO_6$ thick films fabricated by aerosol deposition. Mater Lett 2022; 324:132640.

37. Murugan R, Weppner W, Schmid-Beurmann P, Thangadrai V. Structure and lithium ion conductivity of bismuth containing lithium garnets $Li_5La_3Bi_2O_{12}$ and $Li_6SrLa_2Bi_2O_{12}$. Mater Sci Eng B 2007; 143:14–20.

38. McLachlan D S, Blaszkiewicz M, Newnham R E. Electrical resistivity of composites. J. Am Ceram Soc 1990; 73:2187–2203.

39. Kidner N J, Perry N H, Mason T O. The brick layer model revisited: introducing the nano-grain composite model. J Am Ceram Soc 2008; 91:1733–1746.

TABLE 1. Comparison of densification temperature and total (bulk + grain boundary) ionic conductivity at room temperature (RT) for Na-ion and Li-ion conductive oxide-based solid electrolyte

Materials	Densification Temperature	Total ionic conductivity at RT	References
$Na_2Zn_2TeO_6$	850 ºC	0.63 mS cm^{-1}	7
$Na_2Zn_2TeO_6$	800 ºC	0.40 mS cm^{-1}	12
Na-β'-alumina	1600 ºC	1.67 mS cm^{-1}	16
$Na_{3.4}Zr_2Si_{2.4}P_{0.6}O_{12}$	1250–1300 ºC	4.8 mS cm^{-1}	20
$Na_5YSi_4O_{12}$	1050 ºC	1.59 mS cm^{-1}	21
$Li_{1.4}Al_{0.3}Cr_{0.1}Ti_{1.6}(PO_4)_3$	1070 ºC	1.27 mS cm^{-1}	24
$Li_{1.4}Al_{0.4}Ge_{1.6}(PO_4)_3$	900 ºC	0.34 mS cm^{-1}	25
$Li_{0.29}La_{0.57}TiO_3$	1450 ºC	0.5 mS cm^{-1}	26
$Li_{3/8}Sr_{7/16}Ta_{3/4}Zr_{1/4}O_3$	1300 ºC	0.27 mS cm^{-1}	27
$Li_{6.55}La_3Zr_{1.55}Ta_{0.45}O_{12}$	1150 ºC	0.93 mS cm^{-1}	28
$LiTa_2PO_8$	1050 ºC	0.70 mS cm^{-1}	29

FIGURE CAPTIONS

FIGURE 1. XRD patterns of calcined NZTO powder and hot-pressed NZTO densified under uniaxial pressures of 20 MPa and 60 MPa. Calculated pattern for P2-type NZTO phase is plotted as the reference.[6]

FIGURE 2. SEM images for fractured surface microstructure of NZTO densified under uniaxial pressures of 20 MPa (a) and 60 MPa (b).

FIGURE 3. (A) Nyquist plots of complex impedance at 27ºC for NZTO prepared by FS and HP under uniaxial pressure 60 MPa. Arrhenius plots of total conductivity σ_{total} for both NZTO samples are shown in (B).

FIGURE 4. XRD patterns for NZTO densified by HP under 60 MPa with or without post annealing at 700 ºC and 800 ºC. Calculated patterns for P2-type and O'3-type NZTO phases are also plotted in graph.[6,10]

FIGURE 5. XPS spectra for NZTO densified by HP under 60 MPa with or without post annealing at 800 ºC: (A) spectra in whole measurement range, (B) enlarged C1s peak before post-annealing, (C) enlarged C1s peak after post-annealing.

FIGURE 6. (A) Nyquist plot for complex impedance at 27 ºC for hot-pressed NZTO before and after post-annealing (PA) at 700 ºC and 800 ºC. (B) Calculated R_b and R_{gb} by equivalent circuit fitting for hot-pressed NZTO before and after post-annealing at 700 ºC

and 800 ºC.

FIGURE 7. (A) Bulk and total conductivity at room temperature for hot-pressed NZTO before and after post-annealing at 700 ºC and 800 ºC. The data for NZTO prepared by FS at 800 ºC is also plotted as the reference. (B) Arrhenius plots of total conductivity σ_{total} for hot-pressed NZTO with or without post-annealing.

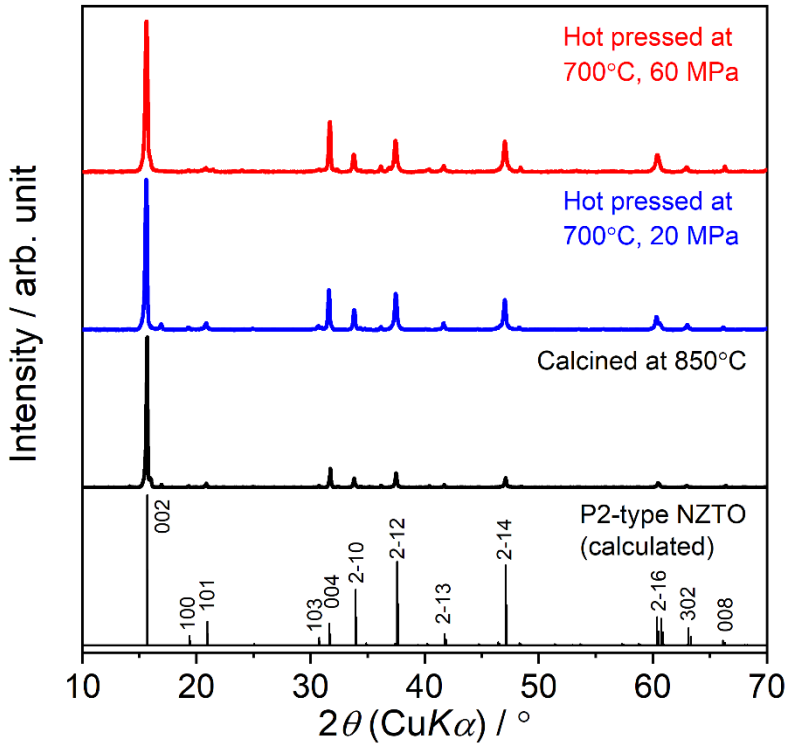

FIGURE 1

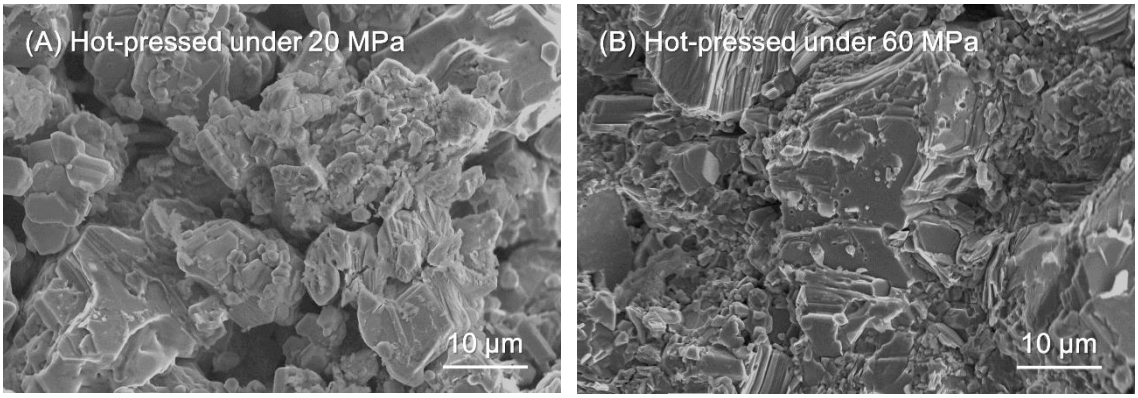

FIGURE 2

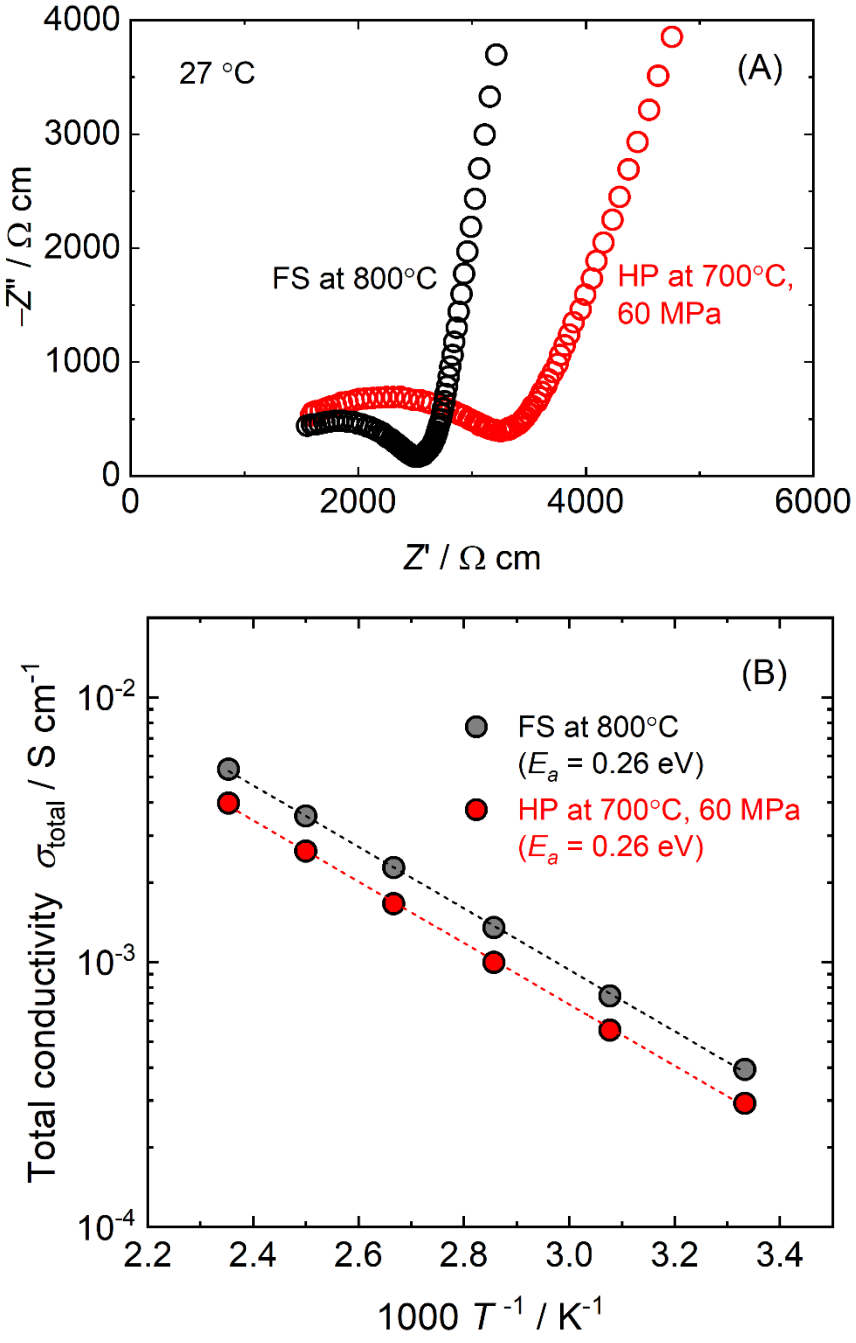
(A)
27 °C
FS at 800°C
HP at 700°C,
60 MPa
–Z'' / Ω cm
Z' / Ω cm
0
1000
2000
3000
4000
0
2000
4000
6000
(B)
FS at 800°C
(E_a = 0.26 eV)
HP at 700°C, 60 MPa
(E_a = 0.26 eV)
Total conductivity σ_{total} / S cm^{-1}
1000 T^{-1} / K^{-1}
10^{-2}
10^{-3}
10^{-4}
2.2
2.4
2.6
2.8
3.0
3.2
3.4

FIGURE 3

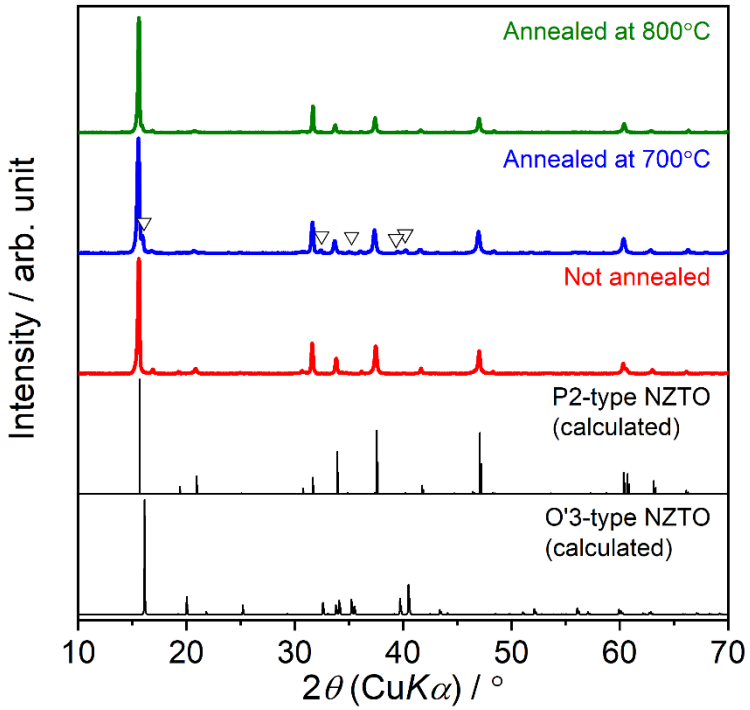

FIGURE 4

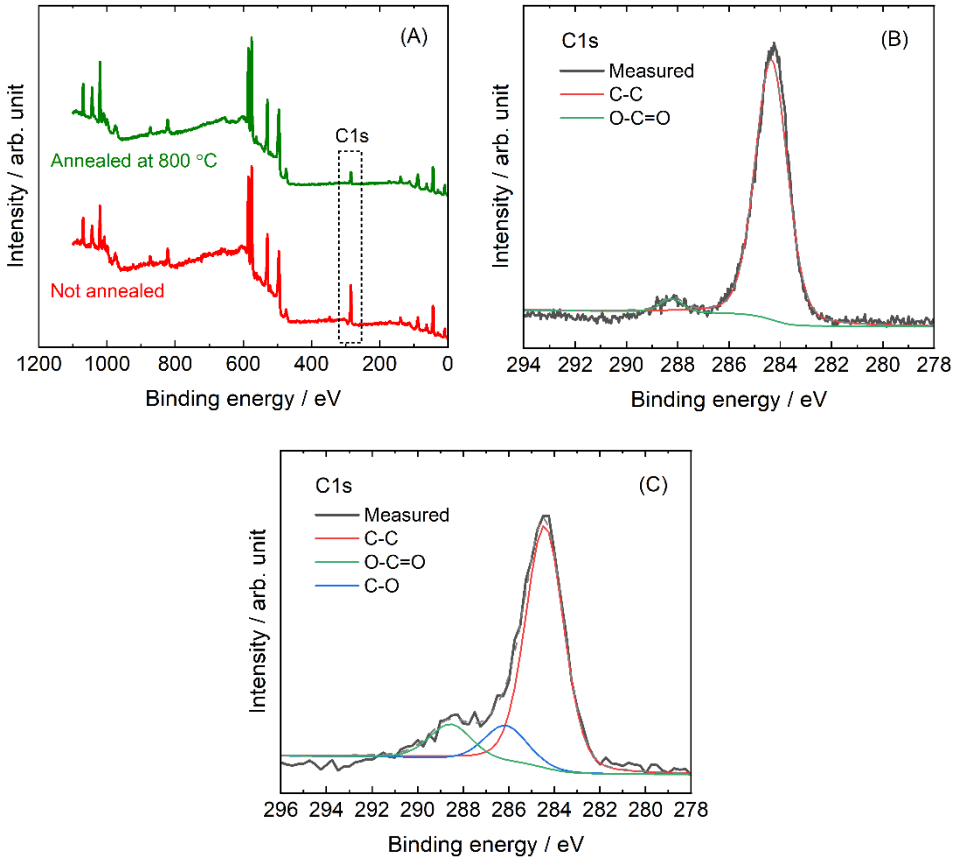

FIGURE 5

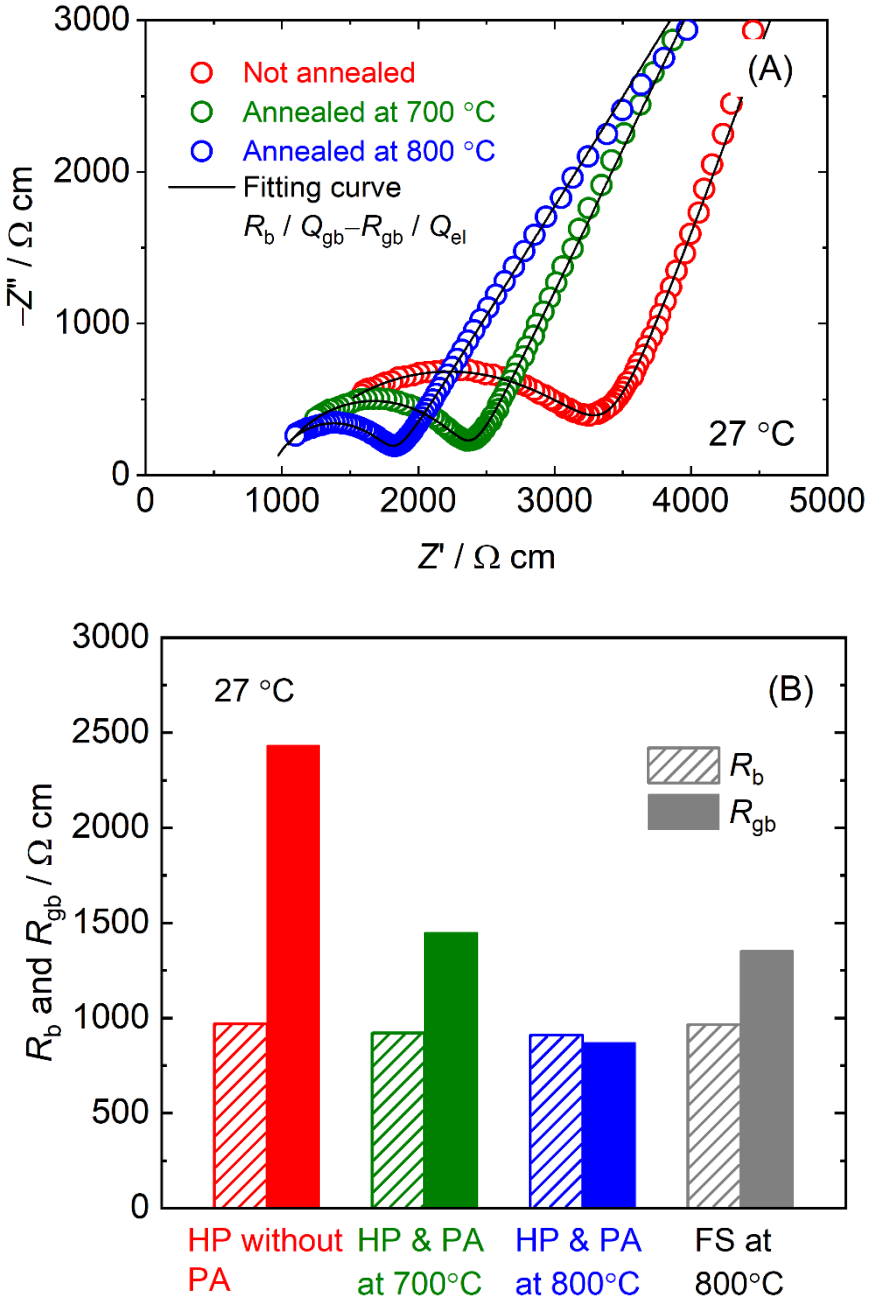
3000
2000
1000
0
0
1000
2000
3000
4000
5000
–Z'' / Ω cm
Z' / Ω cm
Not annealed
Annealed at 700 °C
Annealed at 800 °C
Fitting curve
R_b / Q_{gb}–R_{gb} / Q_{el}
(A)
27 °C
3000
2500
2000
1500
1000
500
0
R_b and R_{gb} / Ω cm
27 °C
(B)
R_b
R_{gb}
HP without PA
HP & PA at 700°C
HP & PA at 800°C
FS at 800°C

FIGURE 6

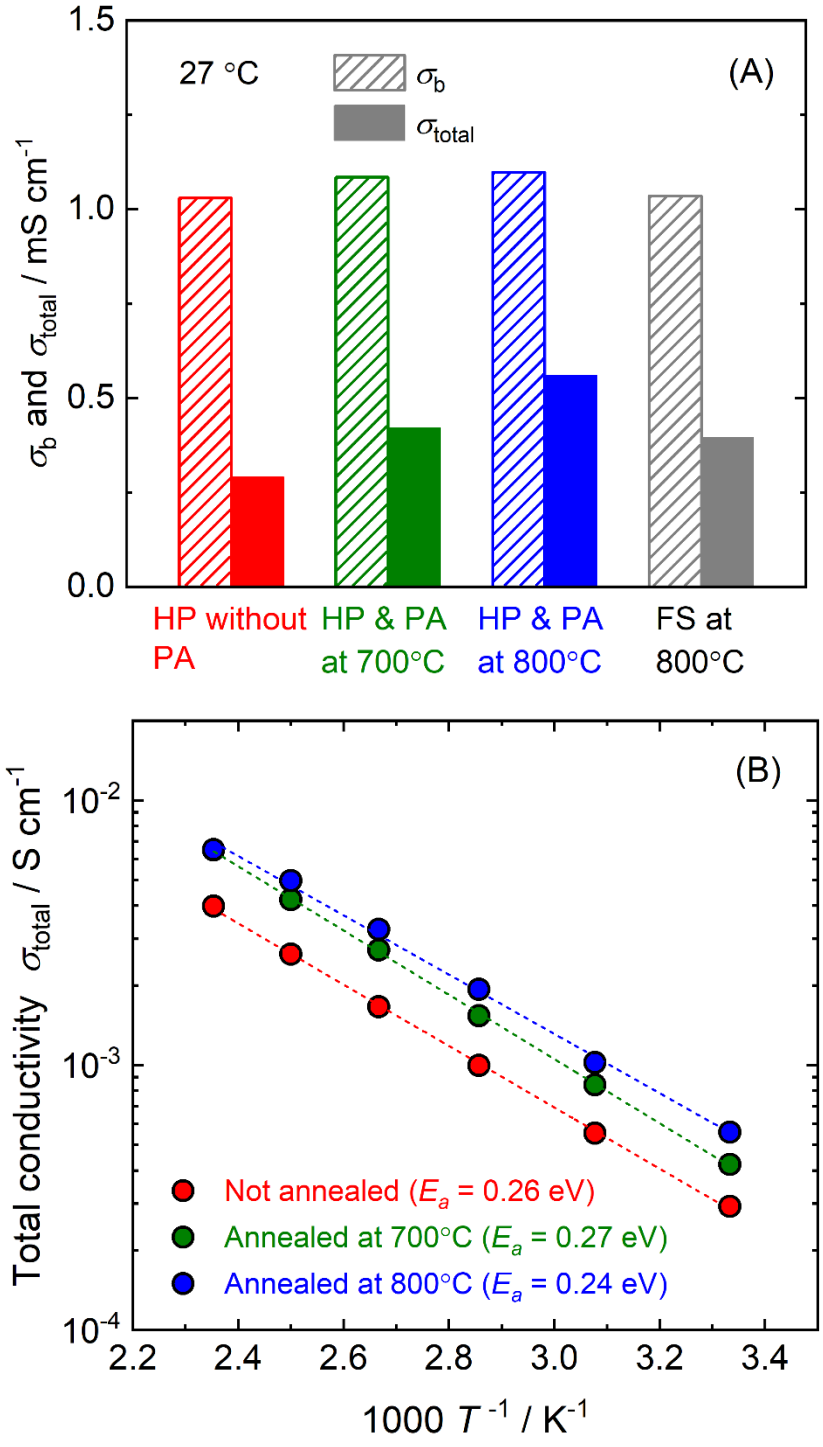
27 °C
σ_b
σ_{total}
(A)
σ_b and σ_{total} / mS cm^{-1}
1.5
1.0
0.5
0.0
HP without PA
HP & PA at 700°C
HP & PA at 800°C
FS at 800°C
(B)
Total conductivity σ_{total} / S cm^{-1}
10^{-2}
10^{-3}
10^{-4}
Not annealed (E_a = 0.26 eV)
Annealed at 700°C (E_a = 0.27 eV)
Annealed at 800°C (E_a = 0.24 eV)
2.2
2.4
2.6
2.8
3.0
3.2
3.4
1000 T^{-1} / K^{-1}

FIGURE 7